ARTICLE

Check for updates

Order−disorder interfaces in a graphitic carbon nitride-nanoclay composite for improved photodynamic antibiotics

Dongyue Wang[1], Qihang Zhao[2,3,4], Aidong Tang[2,3,4] & Huaming Yang ID [1,2,3,4 ✉]

Antibiotic-resistant microorganisms are a threat to human health. Despite efforts to treat bacterial and fungal infections with photodynamic therapy, it suffers from low light absorption and low singlet oxygen yield. Here, we observe order-disorder interfaces in graphitic carbon nitride (g-C_3N_4) modified by kaolinite nanoclay via polar interactions, decreasing the band gap of g-C_3N_4. The polar interactions originate from interactions between the basic amine surface moieties and hydrogen-bonding motifs of g-C_3N_4 and the hydroxyl groups on the nanoclay surface. Surface free energy theory demonstrates that the electron-acceptor displayed by the nanoclay surface could form a couple with g-C_3N_4 due to its nucleophilic property. The polar interactions accelerate electron transfer, and the nanoclay surface functions as an electron sink due to its polar surface and free energy. This promotes spin-orbit coupling and intersystem crossing resulting in a higher singlet oxygen yield, even in the dark. The graphitic carbon nitride-kaolinite composite showed improved and faster would healing in rat animal models.

[1] Hunan Key Laboratory of Mineral Materials and Application, School of Minerals Processing and Bioengineering, Central South University, Changsha 410083, China. [2] Engineering Research Center of Nano-Geomaterials of Ministry of Education, China University of Geosciences, Wuhan 430074, China. [3] Faculty of Materials Science and Chemistry, China University of Geosciences, Wuhan 430074, China. [4] Key Laboratory of Functional Geomaterials in China Nonmetallic Minerals Industry, China University of Geosciences, Wuhan 430074, China. ✉email: hmyang@csu.edu.cn

Bacterial infections have become increasingly threatening to human health[1]. Traditional methods such as antibiotics can prevent and treat infection[2–4], but antibiotics may induce cytotoxicity and side effects. Overuse of antibiotics leads to bacterial drug resistance. Recent developments in antibiotic-free strategies provide new opportunities to address drug resistance. To better treat bacterial infections, various antibacterial drugs and materials have been developed[5,6]. However, a completely effective and affordable solution is lacking[7]. Therefore, combatting bacterial drug resistance remains an active research area. In contrast to chemotherapy and radiotherapy, photodynamic therapy, and other light-activated antibacterial therapies rely on photosensitizers (PS) and light[8,9]; they are more attractive than conventional therapies because they are less invasive with fewer side effects on normal cells[10]. Photodynamic therapy has been used to treat bacterial and fungal infections for more than three decades[11]. Despite their intrinsic advantages, photodynamic therapy still faces challenges and shortcomings, which limit widespread applications in medicine, e.g., challenges of synthesis and storage, low light absorption, and low yield of triplet and singlet oxygen of PS[12]. The incorporation of a heavy atoms into organic molecules can promote intersystem crossing (ISC) to the triplet state[13–15], but these materials are difficult to synthesize and are expensive. There are also toxicity issues and the use of rare and non-renewable precursors[16]. Therefore, alternative materials with similar or even better properties are needed.

Graphitic carbon nitride (g-C_3N_4) is a metal-free polymeric photocatalyst that is electron-rich with abundant hydrogen and nitrogen atoms for hydrogen-bonding[17]. Furthermore, g-C_3N_4 has physicochemical and thermal stability, high efficiency for visible light absorption, good biocompatibility, and low cost[10,18]. Thus, it has been widely utilized and has gained more attention in research[19–21]. However, g-C_3N_4 has yet to reach its full potential and suffers from high charge recombination, low charge mobility, poor crystallinity, and limited absorption of visible light[22]. Numerous efforts have been conducted to overcome these drawbacks to further enhance its applications and performance[23]. Molecular functionalization strategies via noncovalent interactions originating from the functional groups are based on uncondensed amine moieties (–NH_2) and –C≡N groups. These strategies can tune the electronic structure and network of g-C_3N_4. Therefore, molecular interactions via noncovalent interactions can effectively modify the electron structure and enhance its photodynamic performance.

Natural minerals have been extensively utilized due to their stable physical–chemical properties[24]. For example, kaolinite is a two-dimensional material with the chemical composition of $Al_2Si_2O_5(OH)_4$ and is formed by stacking Al–O octahedral and Si–O tetrahedral structures. Clay has been widely applied to adjust functional materials due to its low cost, large surface area, high stability, abundant hydroxyl groups, and permanent negative charge of kaolinite[25]. Moreover, the nature of surface O vacancies and the number of −OH groups can both be tuned by dehydroxylation. Oxygen vacancies on the kaolinite surface can be formed by removing hydroxyl groups and which can lead to more reactive sites[26–28]. Therefore, hydroxyl groups on the surface of kaolinite can produce/maintain interactions between the polar functional groups of g-C_3N_4 while simultaneously generating oxygen vacancies on the kaolinite surface to enhance the photodynamic properties[29]. The abundance of hydroxyl group and O vacancies on the clay surface can be adjusted and this strategy can enhance its performance and broaden its applications.

Herein, we show that these polar interactions originate from interactions between the basic amine surface moieties and hydrogen-bonding motifs of g-C_3N_4 and the hydroxyl group of nanoclay surface. The polar interactions between g-C_3N_4 and

nanoclay can adjust the morphology and electron structure, which in turn decrease the g-C_3N_4 bandgap. In addition, the polar interactions accelerate the electron transfer as a "bridge", and the nanoclay surface functions as an "electron sink" due to its polar surface free energy (γ^{AB}) to promote spin-orbit coupling (SOC) and intersystem crossing (ISC) and thus reduce the singlet-triplet energy gap (ΔE_{ST}). This in turn results in a higher yield of singlet oxygen, even in the dark. Moreover, the g-C_3N_4 and nanoclay composites exhibit much better wound healing effect and showed the faster healing in vivo wound healing on rats.

Results and discussion

Interactions between graphitic carbon nitric and kaolinite. Graphitic carbon nitride g-C_3N_4 (CN) and graphitic carbon nitride-kaolinite (g-C_3N_4/kaolinite, CNK) composites were prepared through the calcination method (see "Experimental Section")[30]. Urea could interact with hydroxyl groups on the surface of kaolinite during the calcination process (Fig. 1a). In addition, the surface free energy could be adjusted simply by hydroxylation through calcination. The structure of the resulting samples was characterized by X-ray diffraction (XRD). The CNK samples exhibit similar and main phase structures for C_3N_4 in the XRD patterns (Fig. 1b and Supplementary Fig. 1). All samples exhibit two typical diffraction peaks located at 13.1 and 27.3 and are assigned to the (100) and (002) planes, thus representing the in-plane structure of tris-triazine (heptazine) units and interlayer stacking sheets of g-C_3N_4. The peak diffraction of (001) CNK450 and (002) g-C_3N_4 become more intense, indicating that the interplanar structure of CNK450 was affected significantly, and that the interlayer stack became less firm[31]. These data illustrate interactions among the interlayer between the surface of g-C_3N_4 and the surface of kaolinite. The molecular structures of samples were further characterized by Fourier transform infrared (FTIR) spectra.

The band near 810 cm^{-1} corresponds to the out-of-plane structure of heptazine rings (Fig. 1c) while the peaks located between 900 and 1800 cm^{-1} are ascribed to the stretching structure of C–N. The band near 2200 cm^{-1} originates from the stretching mode of CN. Additionally, the broad peaks from 3000 to 3500 cm^{-1} are assigned to the N–H stretching vibrations[17]. These observations imply that the CNK samples have similar functional groups compared to g-C_3N_4. Furthermore, the FTIR of CNK exhibits hydroxyl groups near 912 cm^{-1}, which originate from the kaolinite surface. These data suggest that rich hydroxyl groups from kaolinite and N–H groups from g-C_3N_4 will promote polar interactions between the kaolinite surface and g-C_3N_4 (Supplementary Fig. 2). However, only the structure of g-C_3N_4 is significantly affected by the interactions between g-C_3N_4 and the kaolinite surface.

X-ray photoelectron spectroscopy (XPS) measurements were performed to analyze the interactions. The binding energy of Al, Si, and O all shifted to higher binding energy (Fig. 1d and Supplementary Fig. 3), suggesting that the coordination environment became less stable. The binding energy peak of C and N also shifts to a higher binding energy, demonstrating that the electronic structural perturbation leads to different interactions at their interface. The XPS spectrum of C 1s is divided into three distinct peaks around the binding energies of 284.1, 285.6, and 287.5 eV. These correspond to the C=C/C–C, C–N, and N–C=N species on the g-C_3N_4 respectively. In the N 1s spectrum, the binding energies of 398.6 eV are assigned to C–N=C, and the peak at 399.5 eV corresponds to the N (N–$(C)_3$) groups. The peak at 400.0 eV represents the N–H functional groups. While the N 1s peak of CNK450 shifts to lower binding energies versus other samples, indicating a strong interaction between g-C_3N_4 and the surface of kaolinite.
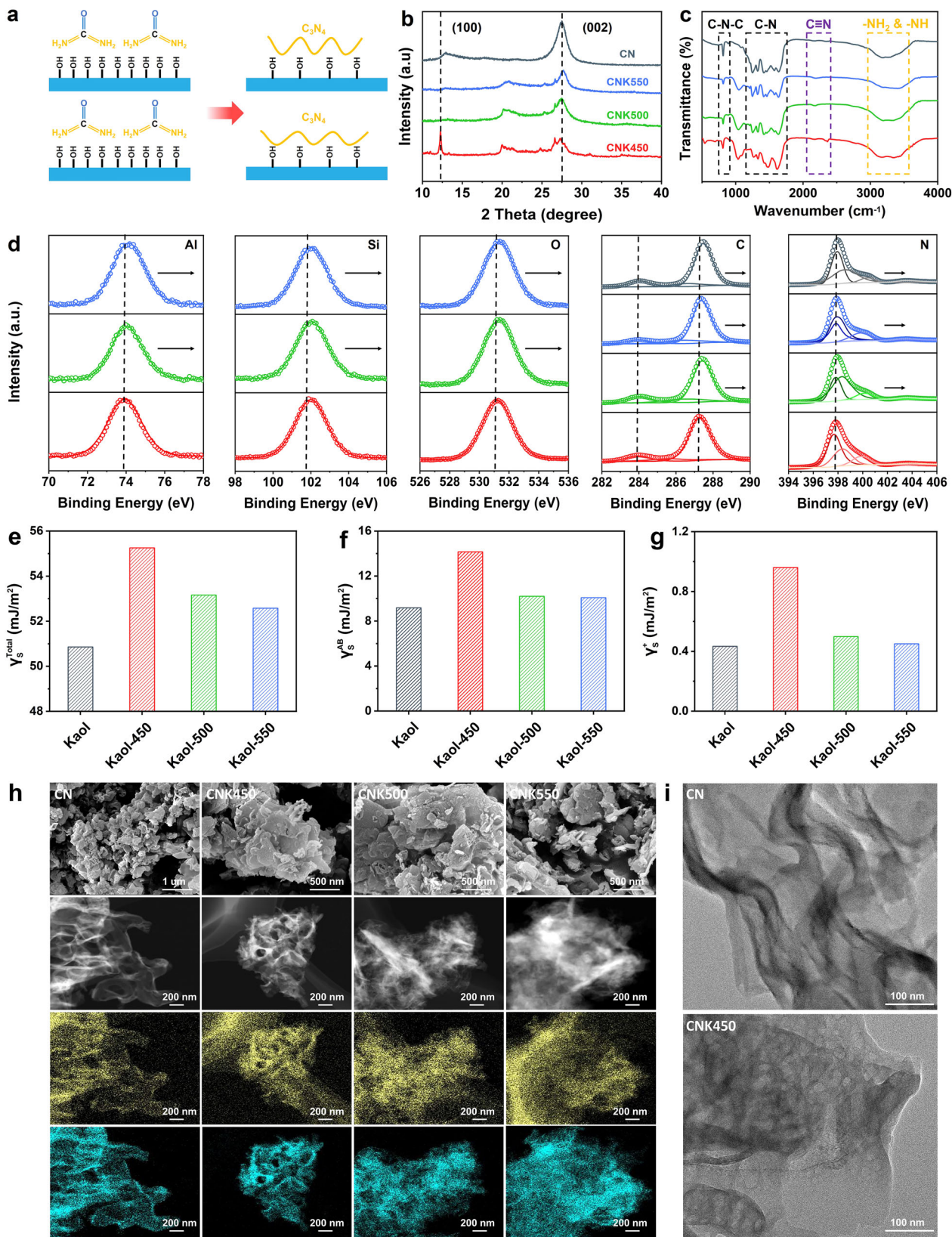
Fig. 1 Characterization of different samples. a Schematic of the sample preparation. **b** XRD patterns. **c** FTIR spectra. **d** Al, Si, O, C, and N XPS spectra of CNK450, CNK500, CNK550, and CN (inset arrow represents the peak shift). Surface free energy of **e** total surface free energy, **f** Lewis acid-base surface free energy, and **g** Lewis acid surface free energy. **h** Typical SEM and TEM images with the distribution of the mapping images of CNK450, CNK500, CNK550, and CN. **i** HRTEM images of CN and CNK450 morphology.

The surface free energy was determined to investigate the formation of interfacial interactions according to the van Oss–Chaudhury–Good theory (Supplementary Fig. 4 and Supplementary Table 1). The total surface free energy γ is composed of two parts: the non-polar part γ^{LW} (i.e., Lifshitz–van der Waals) and the polar part γ^{AB} (i.e., Lewis acid-base)[32,33]. The non-polar dispersive component is mainly attributed to the orientation force (Keesom), the induction force (Debye), and the dispersion force (London forces). The polar component (Lewis acid-base interactions) is mainly associated with the electron donor-acceptor (i.e., γ^- and γ^+) or the π systems interactions (π-interactions)[34–37]. The value of the total surface free energy (Fig. 1e) and the polar surface free energy of CNK450 (Fig. 1f) were higher, while the value of van der Waals surface free energy of CNK450 (Supplementary Fig. 4) is lower than CNK500 and CNK550. This indicates that the surface free energy of CNK450 contributes to the polar interactions between g-C_3N_4 and kaolinite surface. The H-bonding motif and Bronsted basic functional groups of g-C_3N_4 could benefit the polar interactions with the polar surface of kaolinite. This is attributed to the Lewis basic and its nucleophilic characteristics. Moreover, the Lewis acid surface free energy γ^+ results illustrate that kaolinite has a better electron acceptor and could promote electron transfer between g-C_3N_4 and kaolinite surface because the surface can accept donated electrons to due to its strong ability of electron acceptor (Fig. 1g). In addition, g-C_3N_4 has polar functional groups that further promote the formation of polar interactions between g-C_3N_4 and the surface of kaolinite. Therefore, the dominant interactions were the polar interactions between kaolinite and g-C_3N_4 in CN450. Non-polar interactions exist in other samples. Scanning electron microscopy (SEM) and transmission electron microscopy (TEM) were used to further investigate the effects of interactions on the morphology of samples. The SEM and TEM images of CN show obvious wrinkles while the CNK450, CNK500, and CNK550 have a planar structure on the surface of kaolinite due to interactions between g-C_3N_4 and the surface of kaolinite (Fig. 1h, i and Supplementary Fig. 5). In addition, the C and N elements are distributed uniformly over all the samples.

The ordered and disordered structure of g-C_3N_4 at the interface. Small-angle X-ray scattering (SAXS) was employed to characterize the morphology and nanostructure of g-C_3N_4 after interactions between g-C_3N_4 and the kaolinite surface to confirm the order-disorder properties at the interface[38,39]. According to SAXS (Fig. 2a), the scattering intensity of the samples increases with interactions increasing, thus indicating that the morphology of the g-C_3N_4 was affected by the interactions. The Kratky scattering plots were utilized to further characterize the samples' structure. The Kratky plots shift to the lower q value, thus suggesting greater dimensions and a higher cross-sectional zone (Fig. 2b). In addition, the Kratky plot of CNK450 exhibits higher scattering intensity[40], suggesting that the interactions of CKN450 result in lower dimensions and a lower cross-sectional zone of g-C_3N_4 versus CN.

Guinier plots were performed to investigate the cross-sectional structure of g-C_3N_4 and further confirm the zone dimensions of g-C_3N_4 morphology induced by the interactions. Rc can be calculated by fitting published equations[41,42], which represent the radii of g-C_3N_4 of the composites (Fig. 2c). Meanwhile, the average size of the g-C_3N_4 composites can be analyzed and characterized by the cross-sectional radius Rc. The Rc of CNK450 is higher than those of other samples, thus indicating that the cross-sectional radius of g-C_3N_4 of CNK450 is higher than those of other samples (Supplementary Fig. 6a). The results are consistent with the pore size evaluated by BET (Supplementary Figs. 6b, 7 and 8).

The scattering intensity of CN and CN450 were fitted according to a generalized empirical three-region Guinier–Porod model with two Guinier regions[40]. This method models the form factor for the non-spherical structure of samples; Rg_1 and Rg_2 are the characteristic length for the short and overall sizes of the scattering samples[38]. The rough surface structure can be represented by the surface fractals where the value of surface fractals lies between 3 and 4 (Fig. 2d, e). CNK450 exhibits higher Rg_1 (34.1) and Rg_2 (224) than those of CN with Rg_1 of 22.4 and Rg_2 of 196, thus suggesting that the cross-sectional radius of CNK450 is higher than that of CN. The surface fractals of CNK450 are 2.34 while the surface fractals of CN are 2.4, thus indicating that CN has a high roughness compared with CNK450. The morphology characteristics of CN and CNK450 are illustrated in Fig. 2f. The interactions between g-C_3N_4 and kaolinite surface can adjust the cross-sectional radius of g-C_3N_4 and surface fractals. Moreover, the SEM and TEM images (Fig. 2g, h) also show that CN has obvious wrinkles while the CNK450 has a planar structure on the surface of the kaolinite; this again confirms the interactions between g-C_3N_4 and kaolinite surface.

To further confirm the effects of interactions on the photoelectrical properties, the UV–vis absorption spectra, photoluminescence (PL) spectra, and photocurrent curves of time of CN and CNK450 were performed. UV–vis spectroscopy shows that CNK450 exhibits greater optical absorption of light and has a redshift in the visible wavelength range versus CN. CNK450 has a reduced bandgap versus CN (Fig. 2i, Supplementary Fig. 9). Additionally, CNK450 composites show a broad PL spectrum with higher intensity from 400–450 nm (Fig. 2j). The peak intensity of CNK450 is lower than CN, indicating that the recombination of photo-generated electron-hole pairs in the CNK450 composites can be effectively hindered. Furthermore, the prompt fluorescence originates from the radiative decay of singlet excitons. The remarkable decrease in PL intensity clearly demonstrates that the singlet excitons relax. Photocurrent response measurements also indicate that the mobility of charge carriers in CNK450 is higher than that of CN (Fig. 2k), thus implying that interactions improve the charge separation and electron transfer versus CN.

Excitonic effects at the order-disorder interface. Next, steady-state fluorescence was performed to study the fluorescence lifetimes to further understand the effects of the order-disorder on the exciton[43]. Time-resolved fluorescence spectra (Fig. 3a) show that CN has a distinctly slower decay in the time-resolved spectra and all the lifetimes of components prolonged (Supplementary Fig. 10) versus CN450. By fitting the decay kinetics, the calculated average time of CN (6.27 ns) is higher than that of CN450 (5.14 ns). The decrease in multiple lifetime components originates from processes such as exciton diffusion, triplet-triplet annihilation, and Förster resonance energy transfer[44,45]. As the radiative decay of singlet excitons could result in the prompt fluorescence, the lowered PL intensity reveal that the population of singlet excitons reduce remarkably. Also, there is a notable decrease in lifetime, thus further indicating that the population of singlet excitons reduced considerably. The results of remarkable intensity and lifetime difference demonstrate that the exist of process that acceleration of nonradiative intersystem crossing promotes more effective conversion from singlet to triplet excitons[46]. Thus, a decrease in lifetime arises from the ordered structure of g-C_3N_4 and the polar interactions between g-C_3N_4 and kaolinite surface. In this case, the analysis demonstrates high triplet-exciton harvesting and markedly enhanced singlet exciton dissociation in CNK450. These features are attributed to the ordered interface
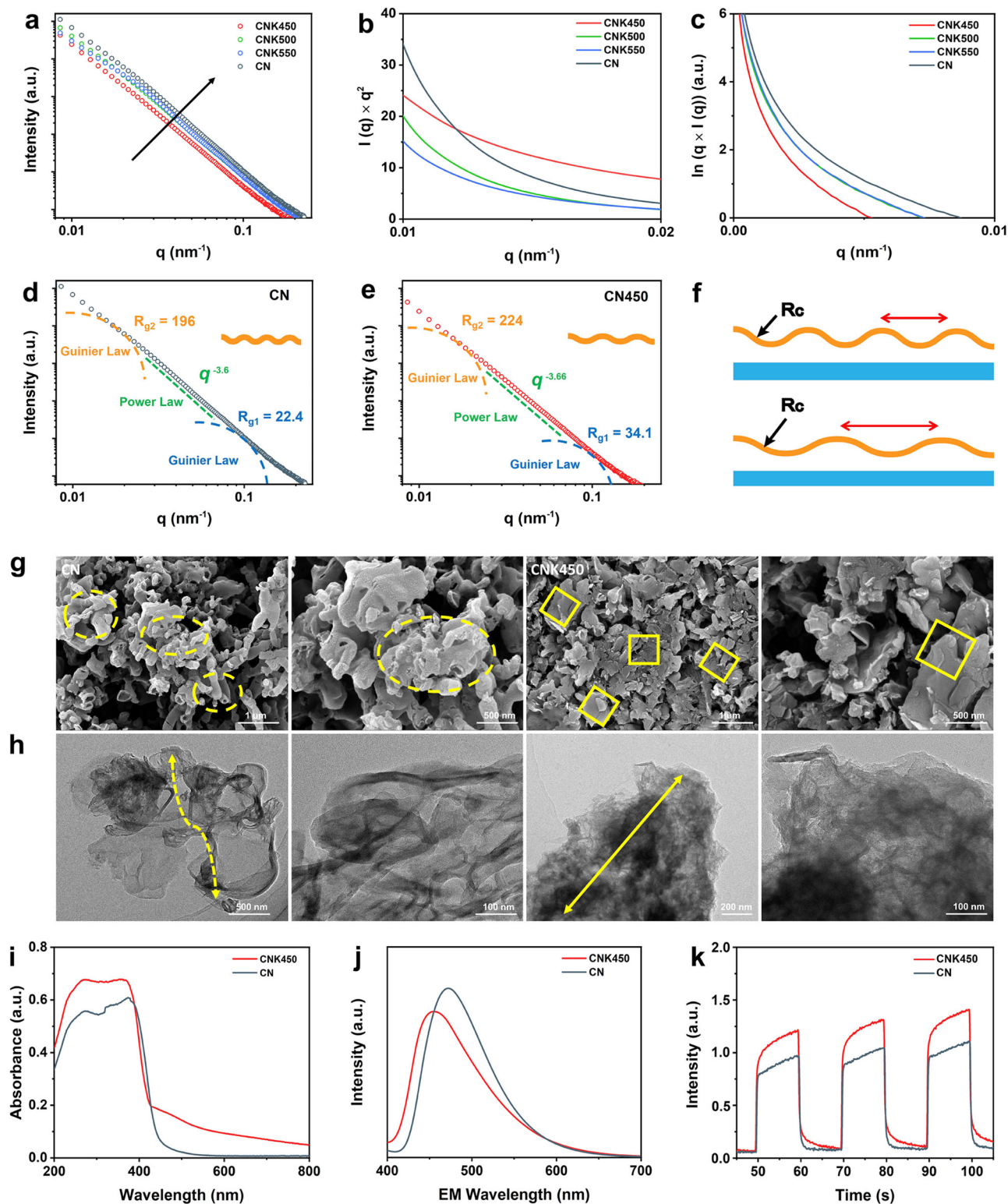
Fig. 2 Structural of g-C$_3$N$_4$ samples and their photoelectrochemical behaviors. a SAXS curves. **b** Kratky plots of the SAXS scattering profiles. **c** Cross-sectional Guinier plots of the SAXS profiles. Fitted SAXS patterns along with schematic representations of the fractal network of CN (**d**) and CNK450 (**e**). **f** Schematic illustration of g-C$_3$N$_4$ morphology. **g** SEM images of CN and CN450 and **h** TEM images of CN and CN450. **i** UV–vis absorption spectra of CN and CN450. **j** Photoluminescence (PL) spectra of CN and CNK. **k** Photocurrent curves over time of CN and CNK. The yellow line represents the morphology of CN and CNK.

arising from polar interactions and trap states, which also promote SOC and reduce ΔE_{ST}[47,48]. The photoluminescence spectra of these materials were studied to further confirm charge transfer and the maximum peak near 380 nm^{-1} was assigned to the delocalized π–π* transition[44]. The CNK450 exhibits a slight redshift to 380 nm^{-1} versus CN (Fig. 3b), indicating that the intramolecular charge transfer of CNK450 was stronger than that of CN. The intensity of the peak redshift also suggests an
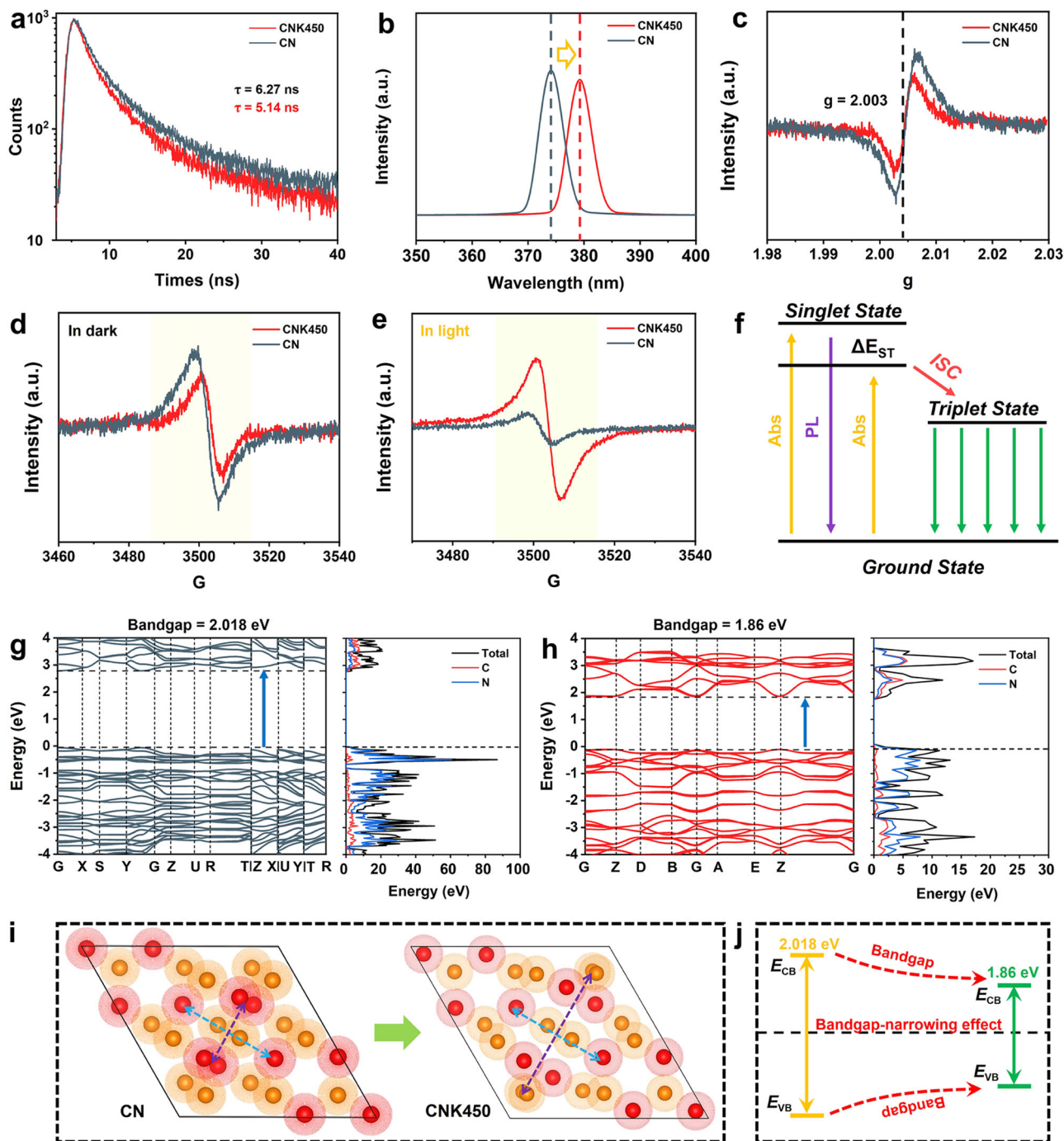
Fig. 3 Mechanism of exciton diffusion and charge transfer process. a Steady-state time-resolved PL spectra. **b** Photoluminescence Emission spectra. (The orange arrow represents the shift of peak). EPR spectra are shown in **c**; EPR spectra in the dark are in **d** and in the light in **e**. **f** Illustration of the charge transfer process of samples. Calculations of band structure and density of states (DOS) of **g** CN and **h** CNK450. **i** Illustrations of the samples' structural change. **j** Samples' bandgap.

intramolecular charge transfer from donor to acceptor[49]. The analysis above demonstrates that the polar interactions improve the charge transfer, which agrees with the surface free energy analysis, PL spectra, and photoelectrical properties. The quantum yields of CN and CNK450 are 4.63% and 3.83%, respectively, thus indicating that the singlet excitons effectively transfer to triplet excitons for CNK450. To further explore the $\pi-\pi^*$ transitions, electron paramagnetic resonance (EPR) measurements were used because the EPR was related to the lone pair electron (Fig. 3c–e). A g value of 2.003 was observed for all samples and was attributed

to the lone pair electron[50,51]. Compared with CN, CNK450 exhibits similar EPR signal intensity in the dark, thus revealing the well-established electronic band structure of g-C_3N_4. However, CNK450 has a much stronger EPR signal intensity than CN, suggesting that the electrons trapped in the kaolinite surface act as a charge-carrier and have shallow trapping states.

The mechanism of the charge transfer process from singlet to triplet is illustrated in Fig. 3f. Density functional theory (DFT) was conducted to calculate the unit structures and electron structures to further illustrate the influence of polar interactions

on the bandgap and charge behavior[52]. The limitations of DFT cause the calculated bandgap value to differ from the experimental value, however, the results of calculations still illustrate the changing trend of bandgap and electron structure[53]. Figure 3g, h shows that the bandgap narrowed from 2.018 eV for CN to 1.86 eV for CNK450, thus indicating a change in g-C_3N_4 morphological structure induced by polar interactions; this plays a key role in the electron structure. The electron density of states (DOS) calculations show that the valence band maximum and conduction band minimum are located at the G point for CN and CNK450 in the Brillouin zone. Furthermore, the electron density of the N states dominates the valence band maximum and conduction band minimum, indicating polar interactions between the –NH_2 functional groups of g-C_3N_4 and the hydroxyl groups of kaolinite surface. This interaction can promote charge transfer as a bridge function. Accordingly, CNK450 presents the stronger adsorption of visible light due to the narrowing bandgap. Figure 3i, j shows the change of g-C_3N_4 structure and bandgap after the polar interactions between the g-C_3N_4 and kaolinite surface based on DFT calculations (Supplementary Fig. 11).

Photodynamic and antibacterial activity. The enhanced SOC and reduced ΔE_{ST} of the samples improve $^1O_2$ generation[4,54]. ROS is responsible for the antibacterial activity of g-C_3N_4, and the antibacterial activity of CN and CNK450 was evaluated in both light and dark. To further identify the singlet oxygen species and photodynamic activity, the antibacterial evaluation and the electron spin resonance (EPR) spectra were conducted to analyze the antibacterial activity and the production of reactive oxygen species. The EPR spectra of all samples exhibit a typical EPR spectrum of three lines with the relative intensity of 1:1:1 in both dark and light (Fig. 4a, b). Furthermore, the signal of CNK450 is dramatically stronger than CN even in the dark, thus indicating that more singlet oxygen species are produced from CNK450 than CN. CNK450 still has relatively higher intensities of singlet oxygen than CN in light. Furthermore, the EPR results in dark and light demonstrate the SOC and reduced ΔE_{ST} of the samples improve $^1O_2$ generation, which agrees well with the structural properties and excitonic effects attributed to polar interactions (Supplementary Fig. 12). In addition, the fluorescence signal of CNK450 exhibit significantly stronger than that of CN, which further proved the strong ability of singlet oxygen production for CNK450 (Supplementary Fig. 13a). Furthermore, the fluorescence imaging studies demonstrate the generation of singlet oxygen, which is the surface-bound reactive oxygen species (Supplementary Fig. 13b). The surface-bound nature of the ROS underlies its selectivity against bacteria over mammalian cells. The surface-bound ROS selectively kill bacteria over mammalian cells[55].

The antibacterial activity of all samples was evaluated by *Escherichia coli* (*E. coli*) because of the prevalence of this species. Antibacterial efficacy against *E. coli* was notably higher in CNK450 (66%) than it was in CN (28%) (Fig. 4c and Supplementary Fig. 14). We next studied the antibacterial mechanism underlying the photodynamic effect via electron microscopy. The morphology and membrane integrity of bacteria was investigated by SEM and TEM. When incubated with samples, the bacteria adsorbed on the surface of the samples and directly interacted with the samples. The samples interact with the bacterial membrane and wrap the bacteria. This improves delivery of more reactive oxygen species to the environment around the bacterial membrane. The typical morphologies of *E. coli* show a relatively smooth surface and rod-like shape (Fig. 4d, e and Supplementary Fig. 15). However, the adsorbed bacteria exposed to CNK450 show a deformed and wrinkled cell wall with a ruptured cell surface. This demonstrates that the singlet oxygen

species were quickly and largely produced, which caused the cell membrane to change and even collapse significantly. The narrowed distance between the samples and bacteria increases ROS efficiency due to the short lifetime of ROS. Therefore, the singlet oxygen species combined with the interactions contributed to the destruction of the bacterial membrane (yellow arrows in Fig. 4e). The bacterial membrane was seriously and obviously damaged when treated with CN450, however these changes were considerably less evident with CN.

Live/dead assays were also performed with laser scanning fluorescence microscopy to further investigate damage to the cell wall. Calcein AM and PI were used to stain *E. coli*. Calcein AM is a cell-permeable green-fluorescent staining the live bacteria, and PI is a cell-impermeable red-fluorescent staining only cells with dead bacteria of damaged membranes. Few dead cells were observed with light relative to control (Fig. 4f). For CN450 in the light-treatment group, many more dead cells were observed relative to CN, and these staining results agree well with the CFU-counting method. As expected, the treated bacteria exhibited much more red fluorescence than CN treatments for CN450 treatment groups, indicating that CNK450 has higher disinfection efficiency and bactericidal activity relative to CN. Taken together, these results demonstrate that the CN450 composite exhibits greater antibacterial activity than pure g-C_3N_4 due to a higher yield of singlet oxygen in CNK450.

In vivo wound healing. The ideal antibacterial materials should exhibit the advantage of good biocompatibility, promoting wound healing and anti-infection. Good biocompatibility is prerequisite for wound-healing materials. The cytocompatibility results in vitro are shown in Supplementary Fig. 16, the cell viability of CNK450 reached almost 90 % within the testing time, even in high concentration of 800 μg mL^{-1} compared with the concentration of 15 μg mL^{-1} of other antibacterial materials, confirming the nontoxic nature and good cytocompatibility of CNK450. Therefore, the good cytocompatibility and antibacterial activity make CNK450 a good candidate material for wound healing. Furthermore, we evaluated further evaluated the in vivo biocompatibility in a rat's infected wound model. The healing promoting property of CNK450 is evaluated using rat's infected wound model and CNK450 was used as the experimental group, while the infected control group received no treatment. The wound was covered with CNK450 sample and fixed by gauze (Fig. 5a). The wound healing was evaluated on day 0, 2, 4, 8, and 14. The traumas are photographed on days 0, 2, 4, 8, and 14. The wound area ratio was utilized to quantitatively evaluate the wound healing rate of CNK450. In addition, wound trace figures were drawn by ImageJ and PowerPoint software. As shown in Fig.5b–d, the wound healing of CNK450 group was significantly better that that of the control group. The experimental group exhibit a faster healing compared with the control group after 4 days treatment (green rectangle). Furthermore, on day 4, the control group still show the obvious inflammation response because the wound size become much larger compared with CNK450. On day 8, CNK450 displayed a smaller size and the wound size decrease significantly than the control group as the dash line indicated. On day 14, the infected wound in the CNK450 group was almost healed completely (the wound closure ratio was ≈ 85%) while the control has wound area ratio of 76%. The results remarkably reveal that CNK450 had much better wound-healing effect than the control group and showed the faster healing. The reason was that CNK450 has a higher yield of ROS, which could kill the bacteria effectively and reduce the inflammation response to promote crawling and proliferation of fibroblastic cells.
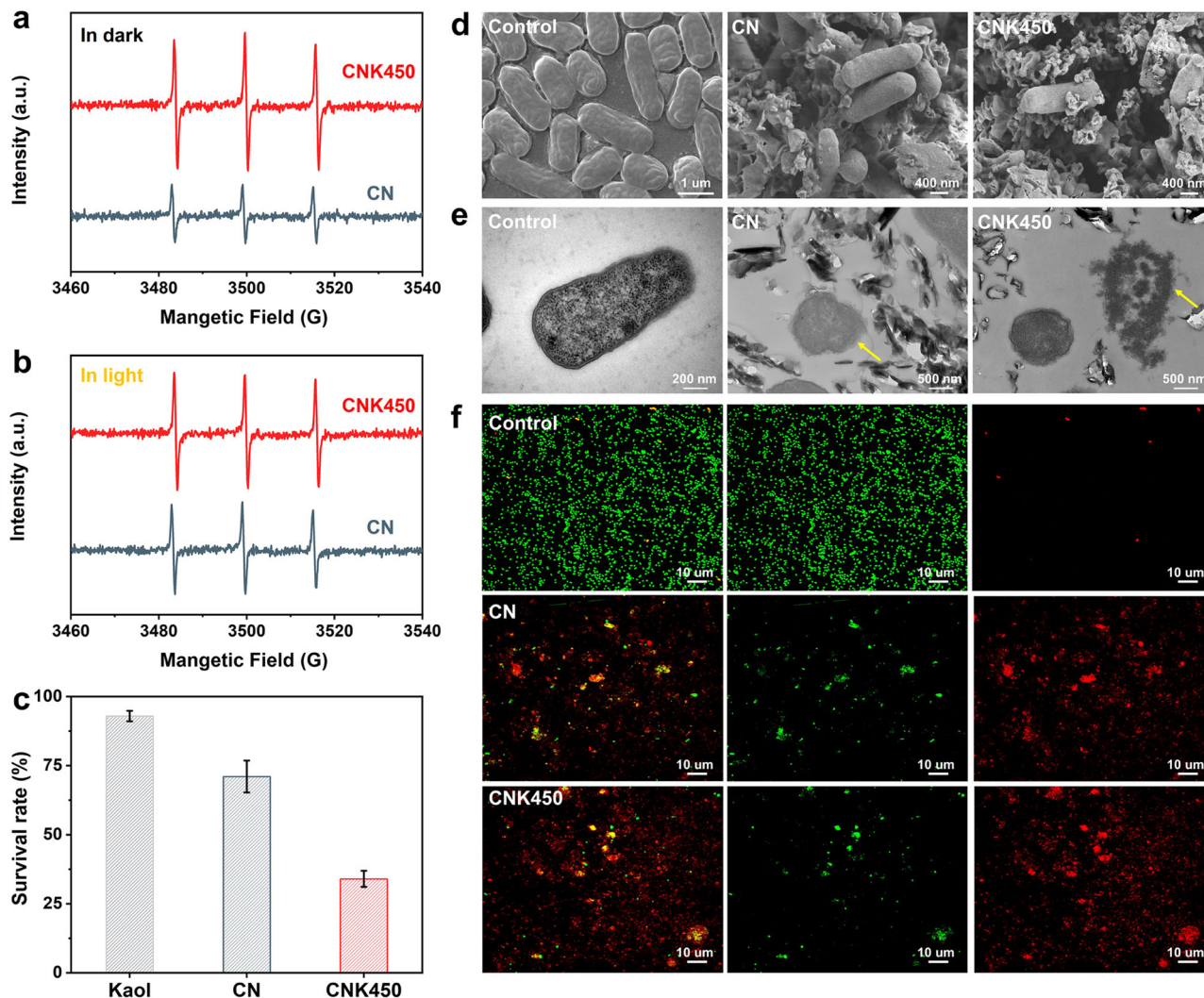
Fig. 4 Identification of singlet oxygen species and mechanism of disinfection mechanism. The EPR spectra of singlet oxygen species of CN and CNK450 **a** in the dark and **b** in the light. **c** Survival rate of *E. coli.* treated with samples in the light. **d** SEM images of *E. coli.* treated with CN and CNK450 samples under visible light. **e** TEM images of *E. coli.* treated with CN and CNK450 samples under visible light. (The yellow arrows indicate the deformed and wrinkled cell wall). **f** Confocal fluorescent images of live and dead *E. coli.* control and treated with CN and CNK450 samples.

Hematoxylin and eosin (H&E) staining is performed to assess the quality of the epidermis, inflammatory reaction and cell proliferation on days 2, 4, 8, and 14. As shown in Fig. 5e, on day 2, obvious neutrophils (red arrows) appear from all the groups, indicating a serious infection and inflammatory response. Meanwhile, a large amount of loose connective tissues is observed in the control group compared with the CNK450 group, indicating that the inflammatory response of the control group was the most serious. On day 4 of HE staining, obvious dermal fibroblasts (green arrows) and newborn blood vessels (cyan arrows) filled with red blood cells are observed from the CNK450 group. The control group still showed a large number of inflammatory cells, indicating the control still exhibit a severe inflammatory response. In sharp contrast, the group of CNK450 had the lightest inflammatory response, indicating the healing effect of CNK450 is better. Meanwhile, the collagen (yellow arrows) in the control groups distributed sparsely compared with the CNK450 group. On day 8, the control group still showed obvious inflammatory response (red arrows) while epidermal healing was achieved for the CNK450 group. On day 15, a large number of tightly-connected fibroblasts are observed for the CNK450 group. On the contrary, inflammatory cells still

existed in the control group, demonstrating that the wound was not fully healed and the healing was insufficient. The results revealed that the infected wounds in the CNK group could reach a satisfactory healing. The healing speed of the CNK450 group was faster than that of the control group by accelerating the formation of fibroblasts tissue. Additionally, Masson staining was employed to evaluate the formation and deposition of collagen in wounds of all groups at different time points (Fig. 5f). On day 2, the deposition of collagen in all groups distributed sparsely. On day 4, a lot of collagen fibers (blue) were observed in the CNK450 groups and exhibited more newly formed collagen. On day 8 and 14, the regenerated collagen obviously increased for all groups. The CNK450 group showed the highest amount of collagen compared with the control group. These results of H&E and Masson staining suggested that the CNK450 could facilitate the process of infected wound healing by accelerating the fibroblasts tissue formation and increasing collagen deposition. Furthermore, the histological analysis of the major organs (heart, liver, spleen, lung, and kidney) of mice does not indicate any abnormal effects or damage after the day 14 treatment (Supplementary Fig. 17), indicating that CNK450 is safe for wound healing.
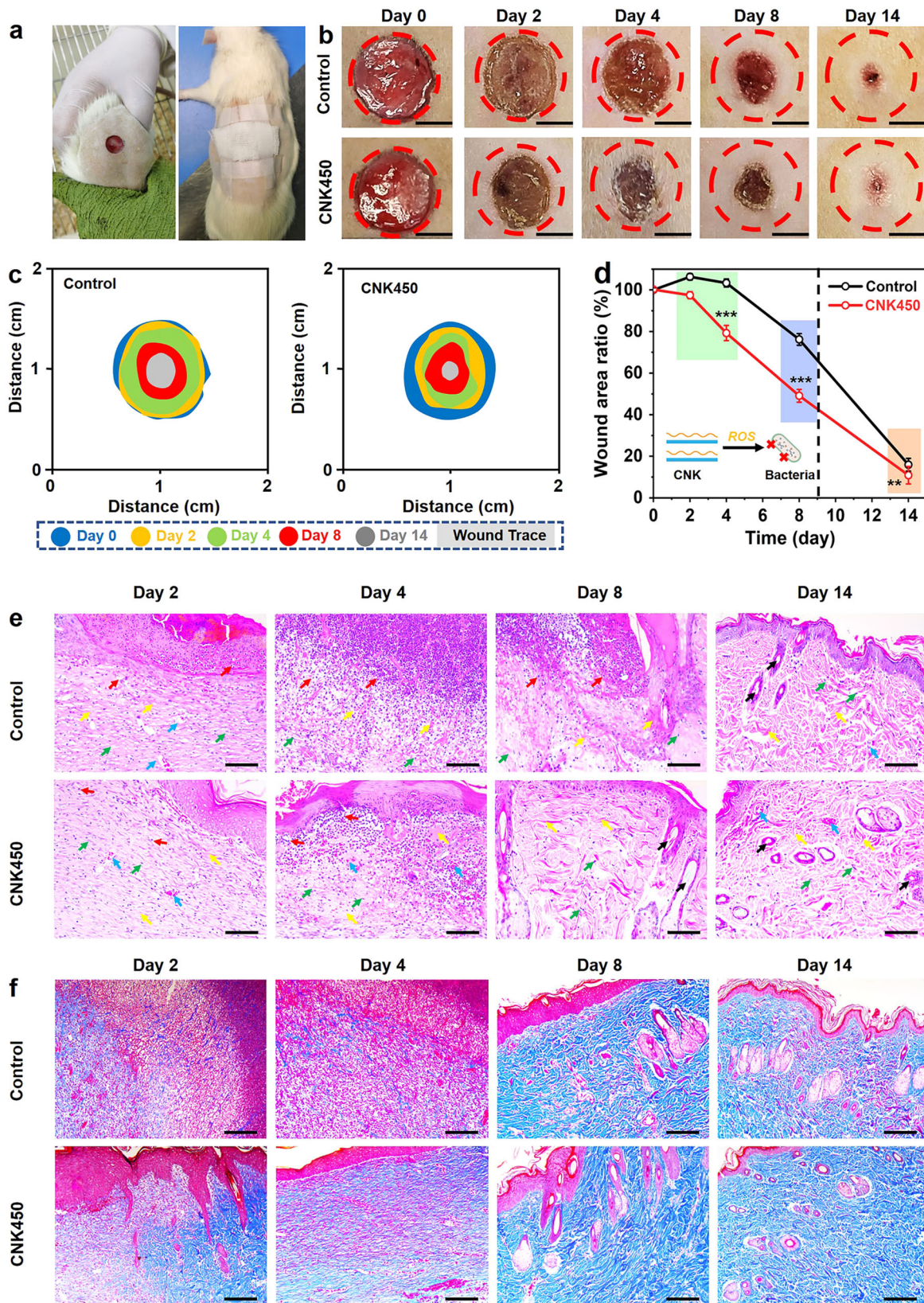
Fig. 5 In vivo anti-infection and bacteria-infected wound healing. a Skin wound images. **b** Representative wound images of wounds in the group of CNK450 and the control group without sample treatment from day 0 to day 14. Scale bar: 10 mm. **c** Wound traces at different periods. **d** Evolution of wound area ratio at different days for each group. The error bars showed standard deviation ($n = 3$), *$p < 0.5$, **$p < 0.01$ or ***$p < 0.001$ (one-way ANOVA followed by Bonferroni's multiple comparison test). The inset image represents the CNK release ROS to kill significantly bacteria during the period as indicated by the dash line. **e** HE staining and **f** Masson staining on day 2, 4, 8 and 14 of the newly regenerated skin tissues for each group. Scale bar: 100 μm.
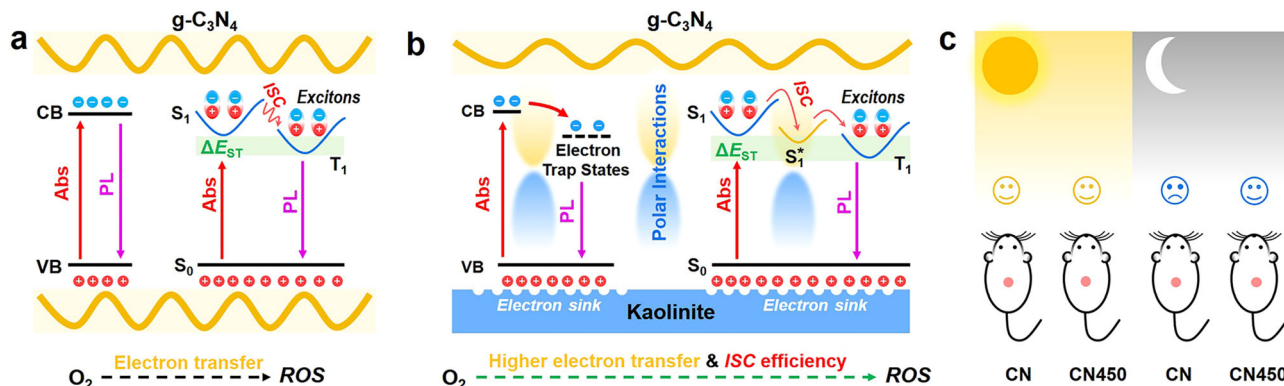
Fig. 6 Schematic description of graphitic carbon nitride-kaolinite's principle of enhancing monolinear oxygen yield and antimicrobial mechanisms. a The charge-carrier-involved mechanisms with "electron trap states" for reactive oxygen generation. **b** The exciton-involved mechanisms with "singlet-excitons trap states" for $^1O_2$ generation. **c** Antimicrobial and wound-healing mechanisms.

Conclusion

This work demonstrates polar interactions could adjust the order-disorder structure at the interface of g-C_3N_4 and kaolinites, resulting from the affinity between the basic amine surface moieties and hydrogen-bonding motifs of g-C_3N_4 and the hydroxyl group of nanoclay surface (Fig. 6). Surface free energy theory further reveal that the affinity attributed to the electron-acceptor displayed by the nanoclay surface could couple with g-C_3N_4 due to its nucleophilic property. The polar interactions induce the changes of the zone dimensions and the cross-sectional structure of the g-C_3N_4 morphology and lead to that the radius (Rc) of g-C_3N_4 in CNK450 is higher than other samples. Therefore, the order-disorder interfaces of g-C_3N_4 could be adjusted by nanoclay via polar interactions, which could decrease the g-C_3N_4 bandgap. The polar interactions also accelerate the electron transfer as a "bridge", with the nanoclay surface functions as an "electron sink" because its polar surface free energy (γ^{AB}) promotes spin-orbit coupling (SOC) and intersystem crossing (ISC) to reduce singlet-triplet energy gaps (ΔE_{ST}). This results in a higher yield of singlet oxygen even in the dark. The above results showed that CNK composites can play a key role in the healing of infected wound and could promote the production of fibroblasts. Meanwhile, the healing of wounds was also accelerated. This work opens paths for photodynamic therapy and may have implications in the fight against antibiotic-resistant bacteria.

Methods

Materials and synthesis. The pristine g-C_3N_4 sample was prepared via thermal polymerization of urea. The 10 g of urea was put in a crucible with a cover, and heated at 550 °C for 3 h. The samples were obtained by washing with ethanol and deionized water three times. The g-C_3N_4/kaolinite composite was prepared by mixing 1 g kaolinite with 10 g urea with complete grinding. The g-C_3N_4/kaolinite composite was placed in a crucible with a cover and heated at different temperatures (450 °C, 500 °C, and 550 °C) for 3 h at 10 °C/min. The samples were then cooled and washed with ethanol and deionized water three times to obtain the products denoted CN (g-C_3N_4), CNK450 (g-C_3N_4/kaolinite 450 °C), CNK500 (g-C_3N_4/kaolinite 500 °C), and CNK550 (g-C_3N_4/kaolinite 550 °C).

Characterizations. Powder X-ray diffraction (XRD) measurements were recorded on a Bruker D8 Advance operating at 40 mA and 40 kV with Cu Kα radiation. TGA used a STA449C instrument at an airflow of 60 mL/min and a heating rate of 5 °C/min. Fourier transform infrared (FTIR) spectroscopy of the samples used a FTIR spectrophotometer (Scientific Nicolet 6700, Thermo Electron Corporation, USA) between 4000 and 400 cm^{-1}. SEM images were taken on a JEOL JSM-7001F field emission scanning electron microscope (JEOL, Japan). HRTEM images and elemental mappings were obtained on an JEM-ARM300F electron microscope (JEOL, Japan). X-ray photoelectron spectroscopy (XPS) studies were carried out on an ESCALAB 250 (Thermo Scientific) using an Al Kα mono chromate (hv = 1486.6 eV) source. Spectra were analyzed using Thermo Scientific Avantage software (Thermo Electron Corporation, USA). The binding energies were calibrated

by the C 1 s peak at 284.6 eV. UV–vis absorption spectra were recorded on a Lambda1050 UV–vis spectrophotometer. The oxygen vacancy of solid samples was measured by Bruker EMXPLUS electron paramagnetic resonance instrument (EPR) (Bruker Scientific Technology Co. Ltd. Germany). N_2 physisorption measurements evaluated the specific surface area and pore structure using the Brunauer-Emmett-Teller (BET) method, and the pore size was determined by the BJH method. Steady-state photoluminescence (PL) spectra were measured on a PE LS55 (HITACHI, Japan) with excitation light at 400 nm. The transient photocurrent performance used a lock-in amplifier (SR 830, Stanford Research Systems, Inc.) with a light chopper (SR540, Stanford Research Systems, Inc.). The scattering patterns were recorded with SAXS from SAXSLAB/XENOCS. The X-ray source is a D2-MetalJet (Excillum) with a liquid metal anode operating at 70 kV and 3.57 mA with Ga-Kα radiation (wavelength λ = 0.1314 nm). The beam was further focused with a focal length of 55 cm using custom-made X-ray optics (Xenocs) to provide a very narrow and intense beam at the sample position.

Electrochemical analysis. The transient photocurrent and electrochemical impedance spectra were collected using catalysts coated on ITO glass via spin coating. The measurements were conducted on a potentiostat CHI660E (Chenhua Co. Ltd. China) via a three-electrode system where Pt wire was the counter electrode, Ag/AgCl was the reference electrode, and a catalyst coated on ITO was the working electrode. Slurry photocurrent measurements were performed in a three-electrode system consisting of Pt wire, a graphite rod, and Ag/AgCl as the working, counter, and reference electrodes, respectively.

Detection and visualization of singlet oxygen generation o the sample surface and in Living Cells. The concentration of singlet oxygen ($^1O_2$) was determined by using an intracellular peroxide-sensitive fluorescent DCFH-DA probe. Bacterial cells were treated with samples for 4 h. After treatment with samples, cells were washed with PBS and then incubated with DCFH- DA (5 μM). The fluorescence intensity was immediately measured at an excitation wavelength of 485 nm and an emission wavelength of 520 nm using a spectrofluorometer PE LS55 (HITACHI, Japan).

Antibacterial activities measurements. The antibacterial activity of samples was assessed with Gram-negative (*E. coli*., ATCC 25922) bacteria. In brief, the pure bacteria in LB were cultivated overnight in a rotating shaker at 37 °C. The bacteria were diluted and spread on agar plates for CFU analysis after treatment for 4 h. In this study, the MIC values were 8.02 mg/mL. Therefore, the dosing concentration of 10 mg/mL was used to incubate *E. coli* for antibacterial activities measurements.

Morphological observation of bacteria. The glutaraldehyde solution (2.5%) was used to fix the bacteria overnight, and the samples were sequentially dehydrated with ethanol solutions (30, 50, 75, 90, 95, and 100%) and vacuum-dried. The morphological images of the bacteria were acquired by SEM and TEM. Each group contained three parallel samples, and at least two sets of images from each sample.

Live/dead bacterial staining assay. A calcein AM/PI double stain kit was used. Here, 20 μL of frozen *E. coli* was added to 20 mL LB medium for 15 h, and then incubated with 0.01 g powdered sample at 37 °C and shaken at 150 rpm for 15 h. After centrifugation at 3000 rpm for 5 min, the supernatant was removed, and the bacterial precipitates were washed with PBS three times. Calcein AM/PI (5 μL) was added to the bacterial suspension (200 μL) and incubated in the dark at 150 rpm for 15 min. The samples were then imaged with a fluorescence microscope (Olympus FV1200).

Computational details. Density functional theory (DFT) calculations were performed with the Vienna Ab Initio Simulation Package (VASP)[56]. The Perdew-Burke-Ernzerhof (PBE) functional was used to treat the exchange-correlation energy, which is based on the generalized gradient approximation (GGA)[57]. A kinetic cutoff energy of 500 eV was employed to describe the ionic cores and expand the plane wave. The width of the Gaussian smearing method for the partial occupancies of the Kohn−Sham orbitals is 0.05 eV. The electronic structure iteration was considered self-consistent when the energy change of the convergence criterion was smaller than 10^{-5} eV. The geometry optimization was considered convergent when the energy change was smaller than 0.02 eV/Å. The Brillouin zone was sampled by 4×4×4 for geometry optimization and $7 \times 7 \times 7$ for static calculation slab structure using a Monkhost–Pack scheme[58]. The strain increment for each deformation step was determined by the biaxial strains with a 10% level of strain up to 30%.

Cytotoxicity testing via MTT assay. L929 cells were grown at 37 °C with 5% CO_2 in dimethyl sulfoxide (DMEM) for 2 days during their logarithmic phase. The cells were harvested by centrifugation at 5000 rpm for 5 min. The cell concentration was adjusted to 10^4–10^5 mL^{-1} (counted with hemocytometers). Next, 100 μL cells were added into every well of a 96-well plate and incubated for 2 h until all cells adhered; the supernatant was then removed and replaced with fresh DMED media or with DMED media with CNK450 (50 μg mL^{-1}, 100 μg mL^{-1}, 200 μg mL^{-1}, 400 μg mL^{-1} and 800 μg mL^{-1}). After 24 h, the supernatant was removed and replaced by 100 μL of PBS. Next, 20 μL of MTT (5 mg mL^{-1} in DMEM) was added into each well, and the cells were incubated at 37 °C for another 4 h to form formazan. Finally, the supernatant with MTT was removed again, and 150 μL of DMSO was added to each well. The cells were incubated for 30 min to dissolve the formazan. The optical density (OD) at 490 nm was monitored, and the cytotoxicity was calculated as the ratio of the OD490 nm in the control experiment divided by the OD490 nm in cytotoxicity experiments. The cytotoxicity enhancement was calculated as the ratio of the cytotoxicity of the composite. Three parallel experiments with L929 cells were performed independently for cytotoxicity testing to evaluate the average OD490 nm and its standard deviation.

In vivo uninfected/infected wound-healing assay. The wound-healing efficacy of the samples was evaluated in Sprague Dawley (SD) male rats weighing 250–300 g. All animal experiments were performed in accordance with the National Institute of Health Guidelines under the protocols, approved by the Animal Ethics Committee of Wuhan Myhalic Biotechnology Co., Ltd. The assigned approval/accreditation number of the laboratory is HLK-20220516-001. All rats were randomly divided into 2 groups: the infected and CNK450. Each group contained 14 rats. The rats were anaesthetized by 10% chloral hydrate (30 mg/kg), and one full-thickness round skin wounds (1 cm diameter) were created on the dorsum of each rat. 100 μL of *E. coli* suspension (1.0×10^8 CFU/mL) was applied to create infected wounds. The wounds became severely infected by 48 h after the addition of the bacterial suspensions. The wound size was measured with Vernier calipers on the 2, 4, 8, and 14-day. The wound closure rate was calculated as follows: wound closure rate (%) = (original wound area - wound area at test time)/ original wound area ×100%. The mice were sacrificed, and the wound tissues were fixed in formalin for paraffin sections. H&E staining and Masson staining were completed, and the samples were then observed and photographed. The major organs including the heart, liver, spleen, lung, and kidney were harvested and stained with H&E after the 14-day treatment.

Statistical analysis. Statistical analysis was carried out using SPSS 9.0 software, and all data were presented as means ± standard deviation (SD). The statistical significance was obtained by one-way ANOVA with Tukey's post hoc test. The differences were considered to be statistically significant for a *p*-value <0.05 (*$P < 0.05$, **$P < 0.01$, ***$P < 0.001$).

Reporting summary. Further information on research design is available in the Nature Research Reporting Summary linked to this article.

Data availability
The data that support the findings of this study and plots within this paper are available from the corresponding authors upon reasonable request.

References
1. Jernigan, J. A. et al. Multidrug-resistant bacterial infections in U.S. hospitalized patients, 2012-2017. *N. Engl. J. Med.* **382**, 1309–1319 (2020).
2. Micoli, F., Bagnoli, F., Rappuoli, R. & Serruto, D. The role of vaccines in combatting antimicrobial resistance. *Nat. Rev. Microbiol.* **19**, 287–302 (2021).
3. Qu, G. et al. Property-activity relationship of black phosphorus at the nano-bio interface: from molecules to organisms. *Chem. Rev.* **120**, 2288–2346 (2020).
4. Yang, B., Chen, Y. & Shi, J. Reactive oxygen species (ROS)-based nanomedicine. *Chem. Rev.* **119**, 4881–4985 (2019).
5. Li, W., Thian, E. S., Wang, M., Wang, Z. & Ren, L. Surface design for antibacterial materials: from fundamentals to advanced strategies. *Adv. Sci.* **8**, e2100368 (2021).
6. De Oliveira, D. M. P. et al. Repurposing a neurodegenerative disease drug to treat Gram-negative antibiotic-resistant bacterial sepsis. *Sci. Transl. Med.* **12**, eabb3791 (2020).
7. Taubes, G. The bacteria fight back. *Science* **321**, 356–361 (2008).
8. Ortiz-Rodriguez, L. A. et al. Electronic relaxation pathways in heavy-atom-free photosensitizers absorbing near-infrared radiation and exhibiting high yields of singlet oxygen generation. *J. Am. Chem. Soc.* **143**, 2676–2681 (2021).
9. Hwang, G. B. et al. Photobactericidal activity activated by thiolated gold nanoclusters at low flux levels of white light. *Nat. Commun.* **11**, 1207 (2020).
10. Zhang, X. et al. Carbon nitride hollow theranostic nanoregulators executing laser-activatable water splitting for enhanced ultrasound/fluorescence imaging and cooperative phototherapy. *ACS Nano* **14**, 4045–4060 (2020).
11. Li, X., Lee, S. & Yoon, J. Supramolecular photosensitizers rejuvenate photodynamic therapy. *Chem. Soc. Rev.* **47**, 1174–1188 (2018).
12. Xu, C., Ravi Anusuyadevi, P., Aymonier, C., Luque, R. & Marre, S. Nanostructured materials for photocatalysis. *Chem. Soc. Rev.* **48**, 3868–3902 (2019).
13. Guo, Q., Zhou, C., Ma, Z. & Yang, X. Fundamentals of TiO_2 photocatalysis: concepts, mechanisms, and challenges. *Adv. Mater.* **31**, e1901997 (2019).
14. Macia, N., Bresoli-Obach, R., Nonell, S. & Heyne, B. Hybrid silver nanocubes for improved plasmon-enhanced singlet oxygen production and inactivation of bacteria. *J. Am. Chem. Soc.* **141**, 684–692 (2019).
15. Han, X. et al. Identifying the activation of bimetallic sites in $NiCo_2S_4$ @g-C_3N_4-CNT hybrid electrocatalysts for synergistic oxygen reduction and evolution. *Adv. Mater.* **31**, e1808281 (2019).
16. Wang, Y., Yang, Y., Shi, Y., Song, H. & Yu, C. Antibiotic-free antibacterial strategies enabled by nanomaterials: progress and perspectives. *Adv. Mater.* **32**, e1904106 (2020).
17. Majdoub, M., Anfar, Z. & Amedlous, A. Emerging chemical functionalization of g-C_3N_4: covalent/noncovalent modifications and applications. *ACS Nano* **14**, 12390–12469 (2020).
18. Gong, L. et al. Carbon nitride-based nanocaptor: an intelligent nanosystem with metal ions chelating e ff ect for enhanced magnetic targeting phototherapy of Alzheimer's disease. *Biomaterials* **267**, 120483 (2021).
19. Villa, K., Manzanares Palenzuela, C. L., Sofer, Z., Matejkova, S. & Pumera, M. Metal-free visible-light photoactivated C_3N_4 bubble-propelled tubular micromotors with inherent fluorescence and on/off capabilities. *ACS Nano* **12**, 12482–12491 (2018).
20. Cui, L. et al. Constructing highly uniform onion-ring-like graphitic carbon nitride for efficient visible-light-driven photocatalytic hydrogen evolution. *ACS Nano* **12**, 5551–5558 (2018).
21. Liu, J. et al. Graphitic carbon nitride (g-C_3N_4)-derived N-rich graphene with tuneable interlayer distance as a high-rate anode for sodium-ion batteries. *Adv. Mater.* **31**, e1901261 (2019).
22. Yu, Y. et al. Surface engineering for extremely enhanced charge separation and photocatalytic hydrogen evolution on g-C_3N_4. *Adv. Mater.* **30**, 1705060 (2018).
23. Wang, H. et al. Boosting hot-electron generation: exciton dissociation at the order-disorder interfaces in polymeric photocatalysts. *J. Am. Chem. Soc.* **139**, 2468–2473 (2017).
24. Dong, X. et al. Monodispersed $CuFe_2O_4$ nanoparticles anchored on natural kaolinite as highly efficient peroxymonosulfate catalyst for bisphenol A degradation. *Appl. Catal. B Environ.* **253**, 206–217 (2019).
25. Sui, X. et al. Advanced support materials and interactions for atomically dispersed noble-metal catalysts: from support effects to design strategies. *Adv. Energy Mater.* **7**, 2102556 (2021).
26. Feng, X. et al. Enhanced dissolution and transformation of ZnO nanoparticles: the role of inositol hexakisphosphate. *Environ. Sci. Technol.* **50**, 5651–5660 (2016).
27. Lakshmi Prasanna, V. & Vijayaraghavan, R. Insight into the mechanism of antibacterial activity of ZnO: surface defects mediated reactive oxygen species even in the dark. *Langmuir* **31**, 9155–9162 (2015).
28. Mudunkotuwa, I. A., Rupasinghe, T., Wu, C. M. & Grassian, V. H. Dissolution of ZnO nanoparticles at circumneutral pH: a study of size effects in the presence and absence of citric acid. *Langmuir* **28**, 396–403 (2012).
29. Zhan, J. et al. Mt-supported ZnO/TiO_2 nanocomposite for agricultural antibacterial agent involving enhanced antibacterial activity and increased wettability. *Appl. Clay Sci.* **214**, 1700286 (2021).

30. Zhao, Q., Fu, L., Jiang, D., Xi, Y. & Yang, H. A nanoclay-induced defective g-C$_3$N$_4$ photocatalyst for highly efficient catalytic reactions. *Chem. Commun.* **54**, 8249–8252 (2018).

31. Kang, Y. et al. Selective breaking of hydrogen bonds of layered carbon nitride for visible light photocatalysis. *Adv. Mater.* **28**, 6471–6477 (2016).

32. Emelyanenko, K. A., Emelyanenko, A. M. & Boinovich, L. B. Van der Waals forces in free and wetting liquid films. *Adv. Colloid Interface Sci.* **269**, 357–369 (2019).

33. Stammitti-Scarpone, A. & Acosta, E. J. Solid-liquid-liquid wettability and its prediction with surface free energy models. *Adv. Colloid Interface Sci.* **264**, 28–46 (2019).

34. Upendar, S., Mani, E. & Basavaraj, M. G. Aggregation and stabilization of colloidal spheroids by oppositely charged spherical nanoparticles. *Langmuir* **34**, 6511–6521 (2018).

35. Bal, V. Stability characteristics of nanoparticles in a laminar linear shear flow in the presence of DLVO and Non-DLVO forces. *Langmuir* **35**, 11175–11187 (2019).

36. Tan, Y. C. & Zeng, H. C. Lewis basicity generated by localised charge imbalance in noble metal nanoparticle-embedded defective metal-organic frameworks. *Nat. Commun.* **9**, 4326 (2018).

37. Guo, Z. et al. Metal-Ion-modified black phosphorus with enhanced stability and transistor performance. *Adv. Mater.* **29**, 1703811 (2017).

38. Liu, Y. et al. A SAXS study of the pore structure evolution in biochar during gasification in H$_2$O, CO$_2$ and H$_2$O/CO$_2$. *Fuel* **292**, 120384 (2021).

39. Prehal, C. et al. Persistent and reversible solid iodine electrodeposition in nanoporous carbons. *Nat. Commun.* **11**, 4838 (2020).

40. Li, H. et al. Macro- and microstructural evolution during drying of regenerated cellulose beads. *ACS Nano* **14**, 6774–6784 (2020).

41. Li, Y. et al. Regulating pore structure of hierarchical porous waste cork-derived hard carbon anode for enhanced na storage performance. *Adv. Energy Mater.* **9**, 1902852 (2019).

42. Anaraki, N. I. et al. New approach for time-resolved and dynamic investigations on nanoparticles agglomeration. *Nano Res.* **13**, 2847–2856 (2020).

43. Zhao, X. et al. Oxygen-dependent regulation of excited-state deactivation process of rational photosensitizer for smart phototherapy. *J. Am. Chem. Soc.* **142**, 1510–1517 (2020).

44. Karthik, D. et al. Acceptor-donor-acceptor-type orange-red thermally activated delayed fluorescence materials realizing external quantum efficiency over 30% with low efficiency roll-off. *Adv. Mater.* **33**, e2007724 (2021).

45. Wu, Y. A. et al. Facet-dependent active sites of a single Cu$_2$O particle photocatalyst for CO$_2$ reduction to methanol. *Nat. Energy* **4**, 957–968 (2019).

46. Fu, J., Yu, J., Jiang, C. & Cheng, B. g-C$_3$N$_4$-based heterostructured photocatalysts. *Adv. Energy Mater.* **8**, 1701503 (2018).

47. Shi, L. et al. Drastic enhancement of photocatalytic activities over phosphoric acid protonated porous g-C$_3$N$_4$ nanosheets under visible light. *Small* **12**, 4431–4439 (2016).

48. Bian, W. et al. Direct identification of surface defects and their influence on the optical characteristics of upconversion nanoparticles. *ACS Nano* **12**, 3623–3628 (2018).

49. Mishra, A. et al. Graphitic carbon nitride (g-C$_3$N$_4$)–based metal-free photocatalysts for water splitting: a review. *Carbon* **149**, 693–721 (2019).

50. Chung, S., Revia, R. A. & Zhang, M. Graphene quantum dots and their applications in bioimaging, biosensing, and therapy. *Adv. Mater.* **33**, e1904362 (2021).

51. Yu, Y. et al. Recent advances in delivery of photosensitive metal-based drugs. *Coord. Chem. Rev.* **387**, 154–179 (2019).

52. Li, J. et al. Zinc-doped Prussian blue enhances photothermal clearance of Staphylococcus aureus and promotes tissue repair in infected wounds. *Nat. Commun.* **10**, 4490 (2019).

53. Zhang, P. et al. Modified carbon nitride nanozyme as bifunctional glucose oxidase-peroxidase for metal-free bioinspired cascade photocatalysis. *Nat. Commun.* **10**, 940 (2019).

54. Chen, S. et al. Oxygen vacancy associated single-electron transfer for photofixation of CO$_2$ to long-chain chemicals. *Nat. Commun.* **10**, 788 (2019).

55. Gao, F., Shao, T., Yu, Y., Xiong, Y. & Yang, L. Surface-bound reactive oxygen species generating nanozymes for selective antibacterial action. *Nat. Commun.* **12**, 745 (2021).

56. Kresse, G. & Furthmuller, J. Efficient iterative schemes for ab initio total-energy calculations using a plane-wave basis set. *Phys. Rev. B* **54**, 11169–11186 (1996).

57. Perdew, J. P., Burke, K. & Ernzerhof, M. Generalized gradient approximation made simple. *Phys. Rev. Lett.* **77**, 3865–3868 (1996).

58. Methfessel, M. & Paxton, A. T. High-precision sampling for Brillouin-zone integration in metals. *Phys. Rev. B* **40**, 3616–3621 (1989).

Acknowledgements

Author contributions

H.Y. conceived the project. D.W. wrote initial drafts of the work. H.Y. wrote the final paper. D.W. designed the experiments, synthesized, and characterized the materials. D.W., Q.Z., and A.T. analyzed the data. All authors discussed the results and commented on the manuscript.

Competing interests

The authors declare no competing interests.

Additional information

Supplementary information The online version contains supplementary material available at https://doi.org/10.1038/s43246-022-00301-y.

Correspondence and requests for materials should be addressed to Huaming Yang.

Peer review information *Communications Materials* thanks Fu Wang and the other, anonymous, reviewer(s) for their contribution to the peer review of this work. Primary Handling Editor: John Plummer.

Reprints and permission information is available at http://www.nature.com/reprints

Publisher's note Springer Nature remains neutral with regard to jurisdictional claims in published maps and institutional affiliations.